International Journal of Applied Science and Engineering
2003. 1, 1: 17-29

The Strain-Space Consistent Tangent Operator and Return Mapping Algorithm for Constitutive Modeling of Confined Concrete

Yi-Ming Lan [a], Elisa D. Sotelino [b], and Wai-Fah Chen [c*]

[a] *Department of Structures and Transportation, Lin Engineering, LTD., Springfield, Illinois, U.S.A.*
[b] *School of Civil Engineering, PurdueUniversity, West Lafayette, Indiana, U.S.A.*
[c] *College of Engineering, University of Hawaii, Honolulu, Hawaii, U.S.A.*

Abstract: Consistent tangent operators with return mapping algorithms in computational mechanics have been recognized to provide accurate and efficient integration for constitutive modeling. Unlike other studies formulated in stress space, the present consistent tangent operator and return mapping scheme have been derived in strain space for hydrostatic-sensitive and nonlinear bounding surface plasticity, particularly the Drucker-Prager criterion with isotropic hardening rule. The developed formulation has been applied to a modified confined concrete model, and implemented through the developed finite-element program UMATconc along with other available ABAQUS options. The agreements between the present results and available experimental and numerical results demonstrate the validity of the current development.

Keywords: constitutive modeling; computational mechanics; concrete plasticity.

1. Introduction

In constitutive modeling, the inconsistency between global and local numerical procedures is the key to the computational inefficiency and instability. The incorporation of consistent tangent moduli (global) with return mapping integration techniques (local) has been found to provide fast-convergent, accurate and stable solutions [1-7]. However, in these works the formulations have been developed in stress space, rather than in strain space. The advantage of the strain-space over stress-space formulation for integrating strain-hardening-softening behavior of plasticity models has been well recognized by many researchers [8-16]. This study focuses on the modeling of the compressive hardening and softening behavior of porous solids such as concrete. The strain-space formulation of the return mapping algorithm and consistent tangent operator for pressure-dependent plasticity is thus adopted herein (Section 2).

The majority of the above-mentioned research works involving return mapping schemes and consistent tangent moduli address pressure-independent single-surface plasticity, i.e. the Von Mises (or J_2) yield function. In this study, the return mapping algorithm and consistent tangent operator for hydrostatic-sensitive plasticity is formulated, particularly for the Drucker-Prager yield function, with nonlinear bounding surface and isotropic hardening rule (Sections 3-4). Furthermore, a confined concrete model has been extended and serves as an illustration of the current formulation (Section 5). By comparing

* Corresponding author: E-mail: chenwf@eng.hawaii.edu *Accepted for Publication: Dec. 28, 2002*

the present results with available experimental data and numerical results, the validity of the current development is achieved. Numerical examples of concrete under both low and high confining pressure are presented (Section 6). Finally, conclusions are summarized in Section 7.

2. Strain-space plasticity formulation

2.1. Loading function

For simplicity, this study is concerned only with small-strain rate-independent plasticity, along with smooth yield and plastic potential surfaces and isotropic hardening rule. Based on isotropic hardening rule, subsequent yield surfaces are assumed to change their sizes depending on a loading parameter k, which can be expressed as a function of the accumulated plastic work $k(W_p)$. Consequently, the loading surface F in strain space takes the form

$$F = F(\boldsymbol{\varepsilon}, \boldsymbol{\varepsilon}^p, k(W_p)) = 0 \qquad (1)$$

Using the strain decomposition, Hooke's law is given as:

$$d\boldsymbol{\sigma} = \mathbf{C}^e (d\boldsymbol{\varepsilon} - d\boldsymbol{\varepsilon}^p) \qquad (2)$$

Note that boldface lower-case letters (e.g. $\boldsymbol{\sigma}$, **a**, **b**) denote second-order tensors, whereas boldface capital letters represent fourth-order tensors (e.g. **C**).

2.2. Loading criteria

As recognized by other researchers [8,12,16], the loading conditions corresponding to the loading surface F can be clearly distinguished in strain space, unlike the ambiguity occurs in stress space (see Table 1). That is,

$\frac{\partial F}{\partial \boldsymbol{\varepsilon}} d\boldsymbol{\varepsilon} > 0$ loading (hardening, softening, or perfect plasticity)

$$\frac{\partial F}{\partial \boldsymbol{\varepsilon}} d\boldsymbol{\varepsilon} = 0 \quad \text{neutral loading} \qquad (3)$$

$$\frac{\partial F}{\partial \boldsymbol{\varepsilon}} d\boldsymbol{\varepsilon} < 0 \quad \text{unloading}$$

where $\frac{\partial F}{\partial \boldsymbol{\varepsilon}}$ denotes the normal to the loading surface

Table 1. Comparison of stress-space an strain-space formulations

Formulation	Loading function	Loading condition			Neutral condition	Unloading condition
		Strain hardening	Strain softening	Perfect plasticity		
Stress space	$f = 0$	A > 0	A < 0	A = 0	A = 0	A < 0
Strain space	F = 0	B > 0	B > 0	B > 0	B = 0	B < 0

$$\mathrm{A} = \frac{\partial f}{\partial \sigma} d\sigma$$

$$\mathrm{B} = \frac{\partial F}{\partial \varepsilon} d\varepsilon$$

2.3. Flow rule

Based on the Il'yushin's postulate [11], the work done dW, by external forces in a closed cycle of deformation of an elastoplastic material is always non-negative in strain space, i.e.,

$$dW = \frac{1}{2} d\boldsymbol{\sigma}^p d\boldsymbol{\varepsilon} \geq 0 \tag{4}$$

Also, $dW_p = \boldsymbol{\varepsilon}^e d\boldsymbol{\sigma}^p = \boldsymbol{\sigma} d\boldsymbol{\varepsilon}^p \geq 0$ (see Figure 1) (5)

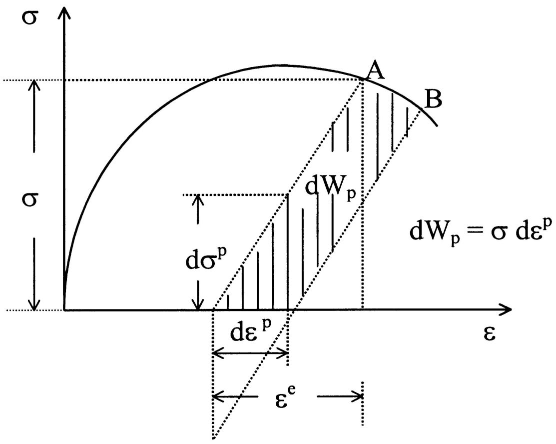

Figure 1. Plastic work increment

where $d\boldsymbol{\sigma}^p$ is known as the *relaxation stress*, and defined in strain space [8] as

$$d\boldsymbol{\sigma}^p = \mathbf{C}^e d\boldsymbol{\varepsilon}^p \tag{6}$$

From Eq. (4), the normality of the relaxation stress on the loading surface F is guaranteed. This leads to the associated flow rule:

$$d\boldsymbol{\sigma}^p = d\lambda \frac{\partial F}{\partial \boldsymbol{\varepsilon}} \tag{7}$$

A more general case can be presented by introducing the plastic potential function G

$$G = G(\boldsymbol{\varepsilon}, \boldsymbol{\varepsilon}^p, k(W_p)) = 0 \tag{8}$$

Similarly, the *nonassociated flow* rule is given as,

$$d\boldsymbol{\sigma}^p = d\lambda \mathbf{r} \tag{9}$$

$$\text{where } \mathbf{r} = \frac{\partial G}{\partial \boldsymbol{\varepsilon}} \tag{10}$$

Substituting Eq. (6) into Eq. (9), the plastic strain increment can be obtained as

$$d\boldsymbol{\varepsilon}^p = d\lambda \mathbf{D}^e \mathbf{r} \tag{11}$$

$$\text{where } \mathbf{D}^e = (\mathbf{C}^e)^{-1} = -\frac{\nu}{E}(\mathbf{1} \otimes \mathbf{1}) + \frac{1}{2\mu}\mathbf{I} \tag{12}$$

3. Return mapping algorithm

The superiority of return mapping algorithms has been well established and recognized by many researchers [17,18,1,6,7]. Like other integration schemes, return mapping algorithms update the stresses and the state variables (e.g. the plastic strains ε^p and the accumulated plastic work W_p), from the typical time step t_n to t_{n+1} at the ith iteration. However, unlike tangent-based schemes which use the state variables at the previous iteration step, return mapping algorithms use those at the previous equilibrium step. This is demonstrated in the following formulation.

First, let $\mathbf{e}_I$ denote the unit tensor field of the elastic deviatoric strain at the end of typical time step [t_n, t_{n+1}], i.e. $\mathbf{e}_I = \dfrac{\mathbf{e}^e}{\|\mathbf{e}^e\|}$ (13)

3.1. Loading surface *F*

For modeling porous materials such as concrete, the Drucker-Prager loading surface f in stress space is often used, and it takes the form

$$f = \alpha I_1 + \sqrt{J_2} - k = 0 \tag{14}$$

where $I_1 = 3p = 3Ktr(\boldsymbol{\varepsilon} - \boldsymbol{\varepsilon}^p)$ (15)

$$J_2 = \frac{1}{2}(\mathbf{s} : \mathbf{s}) = 2\mu^2(\mathbf{e}-\mathbf{e}^p):(\mathbf{e}-\mathbf{e}^p) \tag{16}$$

The loading surface in strain space can be obtained by transforming the loading surface in stress space into strain space. Similar conversions have been adopted by Mizuno and Hatanaka [14] and Farahat et al. [16]. The loading surface F in strain space can thus be obtained as the Drucker-Prager type (see Figure 2), i.e.

$$F = 3K\alpha\bar{I}_1 + 2\mu\sqrt{\bar{J}_2} - k = 0 \tag{17}$$

where $\bar{I}_1 = tr(\boldsymbol{\varepsilon}^e) = tr(\boldsymbol{\varepsilon} - \boldsymbol{\varepsilon}^p)$ (18)

and $\bar{J}_2 = \frac{1}{2}(\mathbf{e} - \mathbf{e}^p) : (\mathbf{e} - \mathbf{e}^p)$ (19)

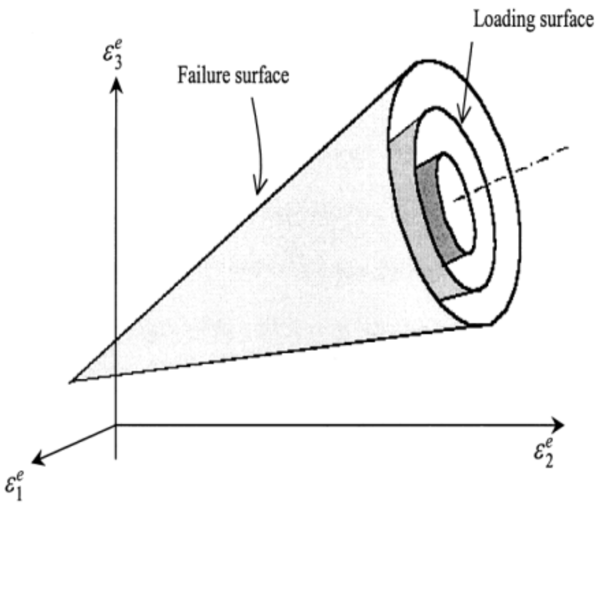

Figure 2. Drucker-Prager loading surfaces in strain space

3.2. Plastic potential surface *G*

The plastic potential surface G is defined in a similar manner as the loading surface F [16], and it is given as

$$G = 3K\alpha\bar{I}_1 + 2\mu C\sqrt{\bar{J}_2} - k = 0 \tag{20}$$

Note that when C = 1, the plastic potential surface G reduces to the loading surface F. Also when C is a constant, it yields linear bounding surface plasticity. If C is a functio of $\bar{I}_1$, it results in nonlinear bounding surface plasticity. For generality, the latter is used in the current formulation with an explicit C.

3.3. Flow rule

Substituting Eqs. (18) and (19) into (20), the plastic potential function G can be obtained as

$$G\left(\boldsymbol{\varepsilon}, \boldsymbol{\varepsilon}^p, k(W_p)\right) = 3K\alpha\left[tr(\boldsymbol{\varepsilon}) - tr(\boldsymbol{\varepsilon}^p)\right] + \sqrt{2}\mu C(\mathbf{e}^e : \mathbf{e}^e)^{\frac{1}{2}} - k(W_p) \tag{21}$$

where $\mathbf{e}^e = \boldsymbol{\varepsilon} - \boldsymbol{\varepsilon}^p - \frac{1}{3}tr(\boldsymbol{\varepsilon} - \boldsymbol{\varepsilon}^p)\mathbf{1}$ (22)

The normal to the nonassociated flow, $\mathbf{r}_{n+1}$, can be stated as

$$\mathbf{r}_{n+1} = \frac{\partial G_{n+1}}{\partial \boldsymbol{\varepsilon}_{n+1}} = 3K\alpha\mathbf{1} + \sqrt{2}\mu C_n \mathbf{e}_I \tag{23}$$

Note that the associated flow is recovered when $C_n = 1$.
Using Eqs. (12) and (23), the plastic strain at the time step t_{n+1} can be represented by

$$\boldsymbol{\varepsilon}_{n+1}^p = \boldsymbol{\varepsilon}_n^p + \Delta\lambda\left(\alpha\mathbf{1} + \frac{C_n}{\sqrt{2}}\mathbf{e}_I\right) \tag{24}$$

Similarly, using Eq. (24) the plastic deviatoric

$$\mathbf{e}^p_{n+1} = \mathbf{e}^p_n + \Delta\lambda \frac{C_n}{\sqrt{2}} \mathbf{e}_I \quad (25)$$

In return mapping algorithms, the given incremental strain is assumed to be all elastic, (see Figure 3).

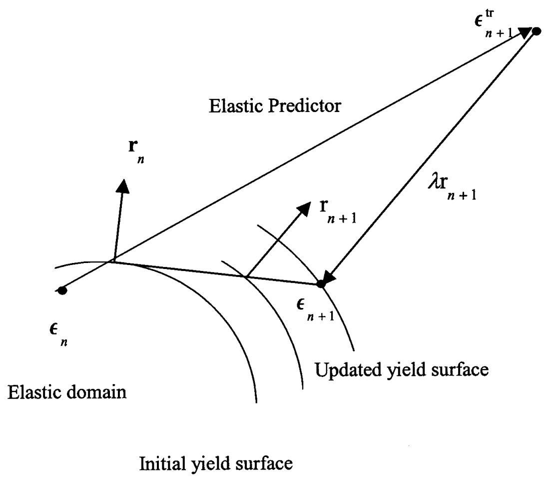

Figure 3. Return mapping algorithm(Generalized Midpoint rule)

Thus, the trial strain takes the form

$$\boldsymbol{\varepsilon}^{tr}_{n+1} = \boldsymbol{\varepsilon}_n + \Delta\boldsymbol{\varepsilon}^{tr}_{n+1} \equiv \boldsymbol{\varepsilon}_n + \Delta\boldsymbol{\varepsilon}_{n+1} \quad (26)$$

Similarly, the trial deviatoric strain is given as

$$\mathbf{e}^{tr}_{n+1} = \mathbf{e}_n + \Delta\mathbf{e}^{tr}_{n+1} \equiv \mathbf{e}_n + \Delta\mathbf{e}_{n+1} \quad (27)$$

and $$\mathbf{e}^{e^{tr}}_{n+1} = \mathbf{e}^e{}_n + \Delta\mathbf{e}^{e^{tr}}_{n+1} \quad (28)$$

Using the strain decomposition, Eqs.(25) and (27), it yields

$$\mathbf{e}^e_{n+1} = \mathbf{e}^{e^{tr}}_{n+1} - \Delta\lambda \frac{C_n}{\sqrt{2}} \mathbf{e}_I \quad (29)$$

Using Eqs. (13) and (29), the following relation can be obtained: strain at time step t_{n+1} can be obtained as

$$\left\|\mathbf{e}^e_{n+1}\right\| = \left\|\mathbf{e}^{e^{tr}}_{n+1}\right\| - \Delta\lambda \frac{C_n}{\sqrt{2}} \quad (30)$$

When $C_n = 1$, the above equation (30) is equivalent to

$$\left\|\mathbf{s}^e_{n+1}\right\| = \left\|\mathbf{s}^{e^{tr}}_{n+1}\right\| - 2\mu\Delta\lambda \quad (31)$$

Similar expressions to Eq. (31) can be found in the derivations of radial-return mapping algorithms for J2 plasticity in stress space [1,19,20]. This indicates, the Von-Mises yield function is recovered.

On the other hand, using Eqs. (24) for $\bar{I}_1$ and Eq. (30) for $\bar{J}_2$, they yields

$$\bar{I}_{1n+1} = tr(\boldsymbol{\varepsilon}_{n+1} - \boldsymbol{\varepsilon}^p_n) - 3\alpha\Delta\lambda \quad (32)$$

$$\bar{J}_{2n+1} = \frac{1}{\sqrt{2}}\left\|\mathbf{e}^{e^{tr}}_{n+1}\right\| - \frac{C_n}{2}\Delta\lambda \quad (33)$$

Also, using the incremental relation the accumulated plastic work W_p results in

$$W_{p_{n+1}}(\Delta\lambda) \cong W_{p_n} + \bar{\boldsymbol{\sigma}}_{n+1} : \Delta\lambda\left(\alpha\mathbf{1} + \frac{C_n}{\sqrt{2}}\mathbf{e}_I\right) \quad (34)$$

where $\bar{\boldsymbol{\sigma}}_{n+1}$ can be treated as the averaged or weighted stress between the current and updated stresses. Iterations can also be used to better estimate the stress $\bar{\boldsymbol{\sigma}}_{n+1}$.

Substituting Eqs. (32) and (33) into Eq. (17), the loading function F can be obtained in terms of $\Delta\lambda$ as

$$F(\Delta\lambda) = 3K\alpha\left[tr(\boldsymbol{\varepsilon}_{n+1} - \boldsymbol{\varepsilon}^p_n) - 3\alpha\Delta\lambda\right] \quad (35)$$

$$+\sqrt{2}\mu\left\|\mathbf{e}^{e^{tr}}_{n+1}\right\| - \mu C_n\Delta\lambda - k\left(W_{p_{n+1}}(\Delta\lambda)\right) = 0$$

where $W_{p_{n+1}}(\Delta\lambda)$ is given in Eq. (34).

Using the above consistency condition Eq. (35), $\Delta\lambda$ can be solved analytically or numerically. The consistency condition can become very complex due to the hardening function k, and the analytical solution may be difficult to obtain or it may not even exist. In the present implementation, numerical methods are employed, particularly, the Van Wijngaarden-Dekker-Brent method.

After solving $\Delta\lambda$, the stress can be consequently updated using Hooke's Law and the strain decomposition, i.e.

$$\boldsymbol{\sigma}_{n+1} = Ktr(\boldsymbol{\varepsilon}_{n+1} - \boldsymbol{\varepsilon}^p_{n+1})\mathbf{1} + 2\mu\mathbf{e}^e_{n+1} \tag{36}$$

Based on the above formulation, the developed return mapping algorithm can be summarized in the following steps:

(i) Compute the trial elastic strains (Eqs. (27) and (28))

$$\Delta\mathbf{e}^{e^{tr}}_{n+1} \equiv \Delta\mathbf{e}^{tr}_{n+1} \equiv \Delta\mathbf{e}_{n+1} = \Delta\boldsymbol{\varepsilon}_{n+1} - \frac{1}{3}tr(\Delta\boldsymbol{\varepsilon}_{n+1})\mathbf{1}$$

$$\text{Where } \Delta\boldsymbol{\varepsilon}_{n+1} = \boldsymbol{\varepsilon}_{n+1} - \boldsymbol{\varepsilon}_n$$

$$\mathbf{e}^{e^{tr}}_{n+1} = \mathbf{e}^e_n + \Delta\mathbf{e}^{e^{tr}}_{n+1}$$

(ii) Compute the return unit tensor field $\mathbf{e}_I$ and the normal $\mathbf{r}$ (Eqs. (13) and (23))

$$\mathbf{e}_I = \frac{\mathbf{e}^{e^{tr}}_{n+1}}{\left\|\mathbf{e}^{e^{tr}}_{n+1}\right\|}$$

$$\mathbf{r}_{n+1} = 3K\alpha\mathbf{1} + \sqrt{2}\mu C_n\mathbf{e}_I$$

(iii) Find $\Delta\lambda$ using the consistency condition (Eq. (35))

$$F(\Delta\lambda) = 3K\alpha\left[tr(\boldsymbol{\varepsilon}_{n+1} - \boldsymbol{\varepsilon}^p_n) - 3\alpha\Delta\lambda\right] + \sqrt{2}\mu\left\|\mathbf{e}^{e^{tr}}_{n+1}\right\| - \mu C_n\Delta\lambda - k\left(W_{p_{n+1}}(\Delta\lambda)\right) = 0$$

(iv) Update the plastic strains and the plastic work (Eqs. (24), (29) and (34))

$$\boldsymbol{\varepsilon}^p_{n+1} = \boldsymbol{\varepsilon}^p_n + \Delta\lambda\left(\alpha\mathbf{1} + \frac{C_n}{\sqrt{2}}\mathbf{e}_I\right)$$

$$\mathbf{e}^e_{n+1} = \mathbf{e}^{e^{tr}}_{n+1} - \Delta\lambda\frac{C_n}{\sqrt{2}}\mathbf{e}_I$$

$$W_{p_{n+1}} \cong W_{p_n} + \overline{\boldsymbol{\sigma}}_{n+1} : \Delta\lambda\left(\alpha\mathbf{1} + \frac{C_n}{\sqrt{2}}\mathbf{e}_I\right)$$

(v) Update the stress (Eq. (36))

$$\boldsymbol{\sigma}_{n+1} = Ktr(\boldsymbol{\varepsilon}_{n+1} - \boldsymbol{\varepsilon}^p_{n+1})\mathbf{1} + 2\mu\mathbf{e}^e_{n+1}$$

4. Consistent tangent operator

In nonlinear finite element analysis, the nonlinear response of a structure is approximated by linear strain paths, incorporated with the incremental-iterative strategies such as the Newton-Raphson method. This method has been widely used in nonlinear analysis, and it is adopted herein.

Assuming the internal nodal-equivalent force vector $\mathbf{N}(\mathbf{d})$ to be a function of the displacement vector $\mathbf{d}$, the tangent stiffness $\mathbf{K}$ may be expressed as

$$\mathbf{K}(\mathbf{d}) = \frac{\partial\mathbf{N}(\mathbf{d})}{\partial\mathbf{d}} \tag{37}$$

Then, $\mathbf{K}$ is the consistent tangent stiffness if

$$\mathbf{K}(\mathbf{d}) = \lim_{\Delta\mathbf{d}\to 0}\frac{\mathbf{N}(\mathbf{d}+\Delta\mathbf{d}) - \mathbf{N}(\mathbf{d})}{\Delta\mathbf{d}} \tag{38}$$

Unlike the continuum tangent operators, the consistent tangent operators are consistent with the integration algorithms used. Such *consistency* preserves the quadratic convergence rate of the Newton-Raphson procedure. This is because the consistent tangent operators evaluate the stress state from the last equilibrium state, while the continuum tangent operators use the state at the end of the previous iterative step. This consistency also allows the consistent tangent operators to detect possible unloading within the iteration step, while the continuum tangent operators are not capable of doing so.

The tangent stiffness operator consistent with the developed return mapping algorithm in strain space is presented next. By substituting Eqs. (24) and (25) into Eq. (36), the stress at n+1 step can be obtained as

$$\boldsymbol{\sigma}_{n+1} = Ktr(\boldsymbol{\varepsilon}_{n+1})1 - Ktr(\boldsymbol{\varepsilon}_n^p)\mathbf{1} - 3K\alpha\Delta\lambda\mathbf{1} + 2\mu\mathbf{e}_{n+1} - 2\mu\mathbf{e}_n^p - \sqrt{2}\mu C_n\Delta\lambda\mathbf{e}_I \quad (39)$$

Hence, the consistent tangent operator can be derived from Eq. (39) as

$$\mathbf{C}^{cp} = \left.\frac{\partial\boldsymbol{\sigma}}{\partial\boldsymbol{\varepsilon}}\right|_{\boldsymbol{\varepsilon}=\boldsymbol{\varepsilon}_{n+1}} = K(\mathbf{1}\otimes\mathbf{1}) - 3K\alpha\boldsymbol{\lambda}^{cp}\mathbf{1} + 2\mu\left[\mathbf{I} - \frac{1}{3}(\mathbf{1}\otimes\mathbf{1})\right] - \sqrt{2}\mu C_n\boldsymbol{\lambda}^{cp}\mathbf{e}_I - \sqrt{2}\mu C_n\Delta\lambda\boldsymbol{\Gamma}^{cp} \quad (40)$$

in which

$$\boldsymbol{\Gamma}^{cp} = \frac{1}{\left\|\mathbf{e}^{e^{tr}}_{n+1}\right\|}\left[\mathbf{I} - \frac{1}{3}(\mathbf{1}\otimes\mathbf{1}) - \mathbf{e}_I\otimes\mathbf{e}_I\right] \quad (41)$$

$$\boldsymbol{\lambda}^{cp} = \frac{3K\alpha\mathbf{1} + \sqrt{2}\mu\mathbf{e}_I - \frac{k'C_n\Delta\lambda}{\sqrt{2}}\boldsymbol{\Gamma}^{cp}\bar{\boldsymbol{\sigma}}_{n+1}}{9K\alpha^2 + \mu C_n + k'\alpha tr(\bar{\boldsymbol{\sigma}}_{n+1}) + \frac{k'C_n}{\sqrt{2}}(\bar{\boldsymbol{\sigma}}_{n+1} : \mathbf{e}_I)} \quad (42)$$

$$k' = \frac{\partial k}{\partial\boldsymbol{\varepsilon}_{n+1}} \quad (43)$$

5. Application to confined concrete

Compressive behavior of concrete is applied here to illustrate the above formulation. The specific material parameters and hardening rule developed from experiments for modeling confined concrete [16] have been adopted. Note that some modifications have been made to the material parameters as well as hardening rule suggested by Farahat et al. [16]. The modifications are made to better simulate confined concrete behavior.

5.1. Material parameters for the failure surface *F* : α , k_0

Two material parameters α and k_0 (max k) for the failure surface F in Eq. (17) can be obtained from available concrete tests [21-24,16]. The compressive meridian of concrete can be assumed to be linear and expressed as

$$a\frac{I_1}{\sqrt{3}f_c'} + \frac{\sqrt{2J_2}}{f_c'} - b = 0 \quad (44)$$

According to the experimental data, material constants a and b can be taken as 0.6736 and 0.445, respectively. By comparing Eq. (44) with the Drucker-Prager failure surface f in Eq. (14), it yields two material parameters α and k_0 to be approximately 0.275 and $0.315 f_c'$, respectively.

5.2. Material parameters for the plastic potential surface *G*: *C*

Let the plastic potential surface G (Eq. (20)) have the same apex as that of the loading surface F. The material parameter C can then be taken as

$$C = \left(1 + \frac{b}{a} - \frac{I_1}{\sqrt{3}f_c'}\right)^m \quad (45)$$

When $I_1 \neq I^f$ $\Rightarrow$ nonlinear bounding surfaces

$I_1 = I^f \quad \Rightarrow$ linear bounding surfaces

$$\text{where } I^f = -(\sigma^f + 2\sigma^N) \tag{46}$$

$$\text{and } \sigma^f = \frac{\sqrt{3}k_0 + (2\sqrt{3}\alpha + 1)\sigma^N}{1-\sqrt{3}\alpha} \tag{47}$$

Note that in the above equation (45), I^f is used by Farahat et al. [16] instead of I_1. In this study, I_1 is modified to preserve the bounding surfaces to be nonlinear for a given confining pressure σ^N, so that concrete dilation behavior under confinement can be better simulated. Also note that when m = 0, the plastic potential surface G coincides with the failure surface F, i.e., $G = F$, as shown in Figure 4, and the associated flow rule is recovered. Also as it can be seen from Figure 4, larger values of m lead to more dilation, and vice versa.

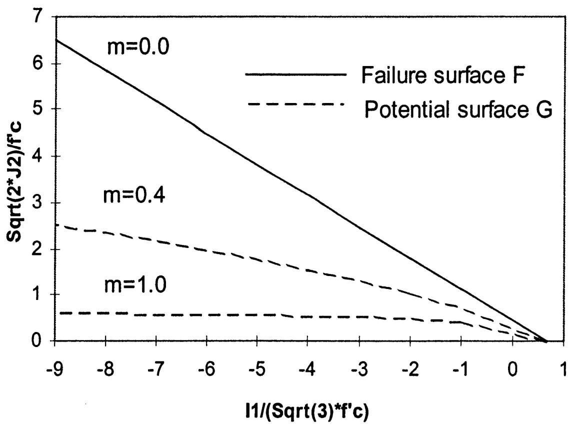

Figure 4. Failure surface *F* and plastic potential surface *G*

5.2. Hardening rule: $k(W_p)$

The hardening rule for confined and unconfined concrete is given as

$$k(W_p) = k_0 \exp\left\{-\left[\left(\beta^N W_p\right)^{\bar{\gamma}} - \xi^N\right]^2\right\} \tag{48}$$

$$\text{where } \beta^N = \beta^u \left[1 - \left(\frac{I^f - I^u}{I^f}\right)^{\bar{\gamma}}\right] A_f \tag{49}$$

$$\xi^N = \xi^u \left[1 + \frac{I^f - I^u}{I^f}\right] \tag{50}$$

$$I^u = -f_c' \tag{51}$$

$$A_f = \frac{(\xi^u)^{\frac{1}{\bar{\gamma}}}}{\beta^u W^0_{ppeak}} \tag{52}$$

(Typically, $W^0_{ppeak} \approx$ 0.03381 MPa, based on Mizuno and Hatanaka [14]).

Note that the amplification factor A_f is not suggested by Farahat et al. [16]. This modification is made to better simulate confined concrete behavior, based on the test results by Mizuno and Hatanaka [14]. The above hardening rule has been defined such that strain-hardening and softening behavior of confined and unconfined concrete can both be represented (see Figure 5). Similar exponential functions for the hardening rule of confined concrete can be found in other studies [12,14].

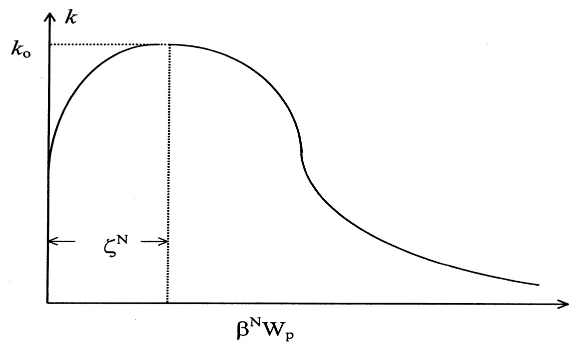

Figure 5. The hardening rule k (as a function of plastic work W_p)

Based on the above k in Eq. (48), the derivative k' in Eq. (43) can be obtained as

$$k' = -2k\bar{\gamma}\left(\beta^N W_p\right)^{\bar{\gamma}-1}\left[\left(\beta^N W_p\right)^{\bar{\gamma}} - \xi^N\right]\beta^N \tag{53}$$

Such k' is to use in computing the consistent tangent operator (Eq. (40)).

6. Numerical examples

The current development is to validate by comparing the present predictions with the available results for concrete under lateral confining pressure. Both low and high confining pressure cases are considered. Unconfined concrete is also studied.

The current results are obtained using the developed finite-element program UMATconc, along with other available ABAQUS options [25]. UMATconc is an ABAQUS user-defined material subroutine served as the implementation of the developed computation procedures along with the above material parameters and hardening rule of the modified concrete model [26]. The current strain-space formulation in fact greatly eased the numerical implementation, since it is also strain-based.Three-dimensional solid elements C3D8 have been used. The Newton-Raphson iterative solution procedure in conjunction with the automatic arc-length (modified Riks) incrementation has also been employed in the following examples.

6.1. Concrete with low confining pressure

The complete loading curves of concrete under low confining pressure are considered. The experimental data conducted by Mizuno and Hatanaka [14] are used. The concrete specimens tested were 10-cm. cubes. The average uniaxial compressive strength was reported 21.2 MPa (3.07 ksi). Three confining pressure cases considered herein are 0, 0.29 MPa (0.042 ksi), and 0.59 MPa (0.086 ksi). Details of the test conditions and procedures can be found in Kosaka et al. [27] and Hatanaka et al. [28].

Like in the tests, two loading steps have been applied in each confinement case. First, a constant confining pressure is applied up to the desired level. Then, the axial compressive load is increased, by superimposing the nodal displacements while maintaining the constant confining pressure in the lateral directions. The current numerical results are based on the material parameters m = 0, $\bar{\gamma}$ = 0.4, along with β^N and ξ^N calculated from Eqs. (49) and (50) for the specific confining pressure σ^N . Figure 6 shows the comparison of the current results with the analytical results of Farahat et al. [16] and the experimental data of Mizuno and Hatanaka [14]. As it can be seen from Figure 6, the current results agree well with the experimental data and numerical results for all three confining cases. The current results show that as the confining pressure increases, the peak stresses and strains increase and the softening branches are less declined. This coincides with the experimental observation that the presence of the confining pressure delays the microcracking process. This example has verified the current formulation.

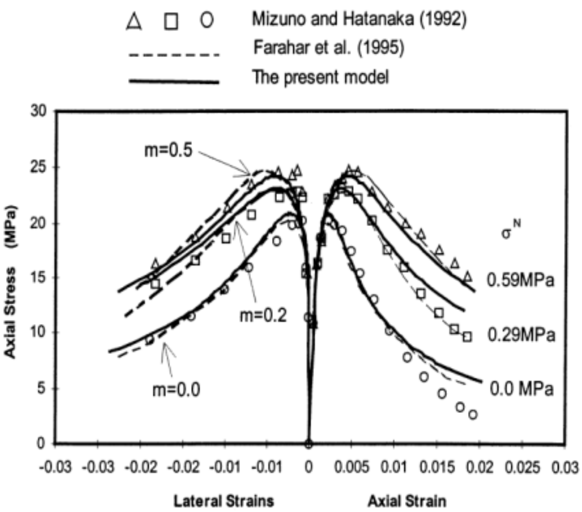

Figure 6. Result comparison for concrete under low confining pressure

6.2. Concrete with high confining presure

Furthermore, the tests conducted by Kotsovos and Newman [29] are studied with high confining pressure. The uniaxial compressive strength is reported to be 47.5 MPa (6.89 ksi). The material parameters used are m = 0.7, $\bar{\gamma}$ = 0.4, along with β^N and ξ^N in

Eqs. (49) and (50). Three cases of constant confining pressure are studied, $0.39f'c$, $0.75f'c$ and $1.1f'c$. Similar to the previous example, two loading steps have been applied for each confining case.

Figure 7 shows the comparison of the current results with the numerical results of Farahat et al. [16] and the experimental data of Kotsovos and Newman [29]. In view of Figure 7, good agreement between the current predictions and the numerical results has been obtained. This again illustrates the validity of the current formulation. Also from Figure 7, the current results agree reasonably well with the test results. The lateral strain hardening and softening, lateral peak strains and peak stresses are all well predicted. However, the results obtained for the peak axial strain are less satisfactory as the confining pressure increases. Similar result is also found by Farahat et al. [16]. This can be attributed to the assumptions made in the present and Farahat's models, such as the loading and the plastic potential functions, as well as the hardening rule.

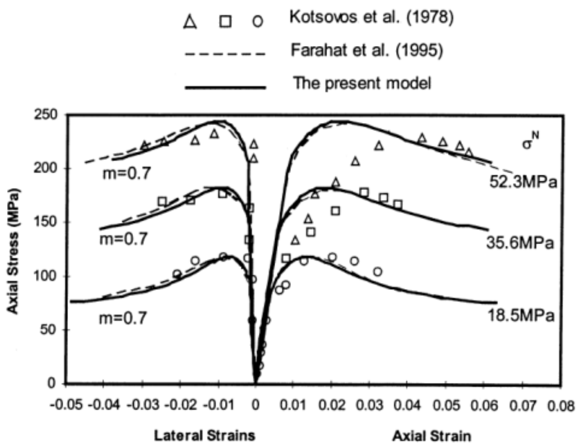

Figure 7. Result comparison for concrete under high confining pressure

The developed constitutive model differs from the model of Farahat et al. [16] primarily on the improvement of the integration algorithm and the tangent stiffness operator. In the present model, the developed return mapping algorithm and consistent tangent operator have been used, whereas the tangent-based scheme and the continuum tangent operator were employed in Farahat's study. The current examples are intended to serve solely as a validation of the developed formulation. The small discrepancy between the current and Farahat's results can be attributed to the modifications made in the present model. More importantly, as expected the complete strain hardening and softening loading curves of confined concrete are traced through the current strain-space formulation.

7. Conclusions

The return mapping algorithm and consistent tangent operator, together known to provide efficient and accurate computations for constitutive modeling, has been derived in strain space for rate-independent hydrostatic-sensitive plasticity with nonlinear bounding surfaces. In particular, the Drucker-Parger yield criterion with isotropic hardening rule is presented. Application of the current formulation to confined concrete behavior has been made. The present results show good agreements with available experimental data and numerical results under both low and high confining pressure. This demonstrates the validity of the current formulation as well as the effectiveness of the proposed modifications to the confined concrete model. Since it is formulated in strain space rather than stress space, the current development can not only predict strain-hardening-softening material behavior, detect possible unloading within the iteration step, but it can also greatly reduced the implementation effort for constitutive modeling, especially when finite-element methods are considered. Finally, the present formulation can be readily extended to other applications involving different porous materials by introducing the appropriate material parameters and hardening rules.

Acknowledgements

The authors are grateful for the financial support from the Purdue Research Foundation under Grant Number 1284-2470.

Appendix notations

A_f = amplification factor

$\boldsymbol{\alpha}^{\varepsilon}$ = back strain tensor

f_c' = concrete compressive strength

σ^N = confining pressure

μ = Lame's constants

$\bar{\gamma}$ = model parameter

k' = partial derivative of k

W_{ppeak}^0 = plastic work constant

W_p = plastic work

ν = Poisson ratio

σ^f = stress variable corresponding to confining pressure σ^N

$\mathbf{D}^e$ = the fourth-order elastic compliance tensor

$\mathbf{e}_I$ = the unit tensor field of the elastic deviatoric strain at the end of typical time step [t_n, t_{n+1}]

$\boldsymbol{\lambda}^{cp}$, $\boldsymbol{\Gamma}^{cp}$ = consistent tangent variables

β^N, ξ^N = model parameters corresponding to confining pressure σ^N

β^u, ξ^u = model parameters corresponding to uniaxial compression

$\mathbf{1}$, $\mathbf{I}$ = the second- and the fourth-order unit tensors, respectively

$d\boldsymbol{\varepsilon}$, $d\boldsymbol{\varepsilon}^e$, $d\boldsymbol{\varepsilon}^p$ = total, elastic and plastic incremental strain tensors, respectively

$I_1, \bar{I}_1$ = the first invariants of stress and strain tensors, respectively

J_2, $\bar{J}_2$ = the second invariants of deviatoric stress and strain tensors, respectively

$\boldsymbol{\sigma}$, $\bar{\boldsymbol{\sigma}}$ = total and averaged stresses, respectively

$d\boldsymbol{\sigma}$, $d\boldsymbol{\sigma}^p$ = total and plastic incremental Cauchy stress tensors, respectively

α, k, k_0, C = material parameters

$\boldsymbol{\varepsilon}, \boldsymbol{\varepsilon}^e, \boldsymbol{\varepsilon}^p$ = total, elastic, and plastic strain tensors, respectively

I^f, I^u = the first invariants of the stress tensor $\boldsymbol{\sigma}$ at failure with and without confinement, respectively

$d\lambda$ = non-negative scalar

$\mathbf{C}^{cp}$ = consistent tangent stiffness

$\mathbf{C}^e$ = the fourth-order elastic moduli tensor

a, b = material constants

$\mathbf{d}$ = displacement vector

dW = work done by external forces

$\mathbf{e}$, $\mathbf{e}^e, \mathbf{e}^p$ = total, elastic, and plastic deviatoric strain tensors, respectively

E, K = Young's and bulk modulus, respectively

F, f = loading functions in strain and stress space, respectively

G, g = plastic potential functions in strain and stress space, respectively

$\mathbf{K}$ = tangent stiffness

m = dilatancy factor ($0 \le m \le 1$)

$\mathbf{N}$ = internal nodal-equivalent force vector

p = hydrostatic stress

$\mathbf{r}$ = the normal to the plastic potential surface G

$\mathbf{s}, \mathbf{s}^e$ = total and elastic deviatoric stress tensors, respectively

t = pseudo time (time step)

Δ = increment

$\| \ \|$ = determinate

$\otimes$ = open product

$:$ = inner or scalar product

$(\ )^{tr}$ = trial variable

$tr(\ )$ = trace operator

$(\ )_n, (\ )_{n+1}$ = at the ith iteration of time step t_n, t_{n+1}, i.e. $(\ )_n^i$, $(\ )_{n+1}^i$, respectively.

References

[1] Simo, L. C. and Taylor, R. L. 1985. Consistent Tangent Operators for Rate-Independent Elastoplasticity, *Computer Methods in Applied Mechanics and Engineering*, 48: 101-118.

[2] Yoder, P. J. and Whirley, R. G. 1984. On the Numerical Implementation of Elastoplastic Models, *Journal of Applied Mechanics*, *Transactions of ASME*, 51: 283-288.

[3] Dodds, R. H. 1987. Numerical Techniques for Plasticity Computations in Finite Element Analysis, *Computers and Structures,* 26, 5: 767-779

[4] Ortiz, M. and Popov, E. P. 1985. Accuracy and Stability of Integration Algorithms for Elastoplastic Constitutive Relations, *International Journal of Numerical Methods in Engineering,* 21: 1561-1576.

[5] Nyssen, C. 1981. An Efficient and Accurate Iterative Method, Allowing Large Incremental Steps, to Solve Elasto-plastic Problems, *Computers and Structures,* 13: 63-71.

[6] Zhang, Z. L. 1995. Explicit Consistent Tangent Moduli with a Return Mapping Algorithm for Pressure-Dependent Elasoplasticity Models, *Computer Methods in Applied Mechanics & Engineering*, 121, 3: 29-44.

[7] Lam, S. S. and Diao, B. 2000. Application of Return Mapping Technique to Multiple Hardening Concrete Model, *Structural Engineering and Mechanics*, 9, 3: 215-226.

[8] Yoder, P. J. and Iwan, W. D. 1981. On the Formulation of Strain-Space Plasticity with Multiple Loading Surfaces, *Journal of Applied Mechanics*, *Transactions of ASME*, 48: 73-778.

[9] Casey, J. and Naghdi, P. M. 1981. On the Characterization of Strain-Hardening in Plasticity, *Journal of Applied Mechanics, Transactions of ASME,* 48: 285-296.

[10] Casey, J. and Naghdi, P. M. 1983. On the Nonequivalence of the Stress-Space and Strain-Space Formulations of Plasticity Theory, *Journal of Applied Mechanics, Transactions of ASME,* 50: 350-354.

[11] Il'yushin, A. A. 1961. On the Postulate of Plasticity, *Journal of Applied Mathematical Mechanics*, 25: 746-752.

[12] Han, D. J. and Chen, W. F., 1985. A Nonuniform Hardening Plasticity Model for Concrete Materials, *Mechanics of Materials,* 4: 285-302.

[13] Kiousis, P. D. 1985. Strain Space Approach for Softening Plasticity, *Journal of Engineering Mechanics,* 113: 210-221.

[14] Mizuno and Hatanaka. 1992. Compressive Softening Model for Concrete*, Journal of Engineering Mechanics*, 118, 8: 1546-1563

[15] Hidaka, E., Farahat A. M., and Ohtsu, M. 1994. Compressive Softening Behavior of Sound and Damaged Concrete Based on a New Strain-Space Plasticity Model, *Transactions of the Japan Concrete Institute,* 16: 95-100.

[16] Farahat, A. M., Kaakami, M., and Ohtsu, M. 1995. Strain-Space Plasticity Model for the Compressive Hardening-Softening Behavior of Concrete*, Construction and Building Materials,* 9, 1: 45-49.

[17] Hughes, T. J. R. 1983. "*Numerical Implementation of Constitutive Models: Rate-Independent Deviatoric Plasticity*", Workshop on Theoretical Foundations for Large Scale Computations of Nonlinear Material Behavior, Northwestern University, Evanston, IL.

[18] Schreyer, H. L., Kulak, R. L., and Kramer, J.M. 1979. Accurate Numerical

Solutions for Elastic-plastic Models, *Pressure Vessel Technology*, *ASME*, 101: 226-234.

[19] Dutta, A. 1992. "*Finite Element Procedures for Inelastic Stability Analysis of Plated Structures*", Ph.D Dissertation, School of Civil Engineering, Purdue University.

[20] Nukala, P. K. V. V. 1997. "*Three-Dimensional Second-Order Inelastic Analysis of Steel Frames*", Ph.D. Dissertation, School of Civil Engineering, Purdue University.

[21] Richard, F. E., Brandtzaeg, A., and Brown, R. L. 1928. "*A Study of The Failure of Concrete Under Combined Compressive Stresses*", University of Illinois Engineering Experimental Station Bulletin 185.

[22] Balmer, G. C. 1949. "*Shear Strength of Concrete under High Triaxial Stress-Computation of Mohr's Envelope as a Curve*", Structural Research Laboratory Report No SP-23, Denver, Colorado, October.

[23] Chinn, J. and Zimmerman, R. M. 1965. "*Behavior of Plain Concrete under Various High Triaxial Compression Loading Conditions*", Technical Report No. WL TR 64-163 (AD 468460), Air Force Weapons Laboratory, New Mexico, August.

[24] Mills, L. L. and Zimmerman, R. M. 1970. Compressive Strength of Plain Concrete under Multiaxial Loading Conditions, *Journal of ACI,* 67: 802-807.

[25] ABAQUS Manuals, Version 5.8.

[26] Lan, Y. M. 1998. "*Finite Element Study of Concrete Columns with Fiber Composite Jackets*", Ph.D. Dissertation, School of Civil Engineering, Purdue University.

[27] Kosaka, Y., Tanigawa, Y., and Hatanaka, S. 1985. Lateral Confining Stresses due to Steel Fibers in Concrete under Compression, *International Journal of Cement Compos*ites and Lightweight Concrete, 7, 2: 81-92.

[28] Hatanaka, S., Kosaka, Y., and Tanigawa, Y. 1987. Plastic Deformational Behavior of Axially Loaded Concrete under Low Lateral Pressure -- An Evaluation Method for Compressive Toughness of Laterally Confined Concretes (Part I), *Journal of Structural Construction Engineering*, Tokyo, Japan, 377: 27-40.

[29] Kotsovos, M. D. and Newman, J. B. 1978. Generalized Stress-Strain Relations for Concrete, *Journal of Engineering Mechanics*, *ASCE*, 104: 845-856.